Interfacial hydration determines orientational and functional dimorphism of sterol-derived Raman tags in lipid-coated nanoparticles

Xingda An[a,b], Ayan Majumder[a], James McNeely[a], Jialing Yang[a,b], Taranee Puri[a], Zhiliang He[a], Taimeng Liang[a], John K. Snyder[a], John E. Straub[a], and Björn M. Reinhard[a,b,1]

[a]Department of Chemistry, Boston University, Boston, MA 02215; and [b]The Photonics Center, Boston University, Boston, MA 02215

Edited by Catherine J. Murphy, University of Illinois at Urbana–Champaign, Urbana, IL, and approved July 6, 2021 (received for review March 27, 2021)

Lipid-coated noble metal nanoparticles (L-NPs) combine the biomimetic surface properties of a self-assembled lipid membrane with the plasmonic properties of a nanoparticle (NP) core. In this work, we investigate derivatives of cholesterol, which can be found in high concentrations in biological membranes, and other terpenoids, as tunable, synthetic platforms to functionalize L-NPs. Side chains of different length and polarity, with a terminal alkyne group as Raman label, are introduced into cholesterol and betulin frameworks. The synthesized tags are shown to coexist in two conformations in the lipid layer of the L-NPs, identified as "head-out" and "head-in" orientations, whose relative ratio is determined by their interactions with the lipid–water hydrogen-bonding network. The orientational dimorphism of the tags introduces orthogonal functionalities into the NP surface for selective targeting and plasmon-enhanced Raman sensing, which is utilized for the identification and Raman imaging of epidermal growth factor receptor–overexpressing cancer cells.

lipid-coated nanoparticles | hydrogen bonding | surface-enhanced Raman spectroscopy | epidermal growth factor | cholesterol

Lipid-coated noble metal nanoparticles (L-NPs) that contain a lipid membrane around a NP core represent an intriguing class of hybrid materials that combine the surface properties of biological membranes with the advantageous material properties and optical responses of a metal NP core (1–5). Depending on their exact composition, lipid membranes can enable the conjugation of specific biomolecules (6), facilitate the mimicry of biological NPs such as exosomes or enveloped viruses (7), engage cellular lipid-binding functionalities and associated signaling pathways (7–9), and provide custom-tailored stealth properties for biomedical applications (10). The noble metal NP core sustains strong size and shape-dependent localized surface plasmon resonances (LSPRs), which give rise to large, optical absorption and scattering cross-sections. The strong electric field (E-field) within the vicinity of the NPs under resonant excitation of the LSPR can enhance the inelastic scattering of molecules localized in the evanescent E-field close to the metal surface. This well-known effect forms the foundation of surface enhanced Raman spectroscopy (SERS) (11, 12). The large electron and X-ray absorption cross-sections also render noble metal NPs versatile and multimodal probes for optical, electron, and X-ray microscopies (13, 14).

Due to their structural similarity with enveloped viruses, L-NPs have been used as model systems for investigating the viral binding and entrance (5, 15), as well as for probing intracellular trafficking pathways (7–9). L-NPs have also been exploited for high-contrast biomolecular imaging (16, 17), for controlled drug or cargo delivery (18, 19), and for plasmon-enhanced pathogen inactivation (20, 21). Importantly, the functionality of L-NPs in specific applications can be determined by the structure and composition of the lipid architectures. For instance, L-NPs intended for targeting cell surface receptors in particle–cell interaction studies (8, 22) or for enhancing photochemical reactions in the ambient medium (4) require targeting ligands or photocatalysts localized in the membrane surface, where they are accessible to the medium. In contrast, optical probe (16, 23) or nanocarrier (18, 21) applications of L-NPs benefit from an integration of optical labels or cargo molecules within the membrane, where they are protected from environmental influences and reactions.

Sterols, in particular cholesterol, and other terpenoid derivatives are important components of L-NPs and, in general, play vital roles in regulating membrane formation (24–26), fluidity (27), phase behavior (28, 29), domain formation (30, 31), permeability (32), and additional physicochemical properties of both biological and artificial lipid architectures. Therefore, chemical derivatization of these essential membrane components presents a promising strategy for controlling the membrane properties of L-NPs. We modify, in this work, cholesterol and betulin to generate three modified tag molecules (Tag-1 to Tag-3) with side chains that differ in polarity and lengths, but all contain a terminal alkyne group, and investigate their integration into L-NPs. The tag structure as well as the solvation properties of the modified side chains impact their interactions with surrounding lipids and water, determine their orientation in the membrane, and thus directly affect the surface chemical properties of the L-NPs. The terminal alkyne provides a platform for bioorthogonal chemical conjugation, as well as a strong and unique Raman signature whose precise stretching frequencies depend on the local chemical environment (33, 34). We probe the orientations of Tag-1 to Tag-3 in the NP-supported lipid membrane,

Significance

Derivatized sterols and terpenoids represent an effective platform for introducing functionality into the surface of lipid-coated NPs and other membrane-based materials. This work demonstrates that the hydrogen-bonding network (HBN) at the lipid–water interface plays a crucial role in determining the orientation of derivatized sterols and other terpenoids in hybrid lipid membranes. A rational engineering of the interactions with the HBN provides control over the molecular orientation in the lipid coating and facilitates configurable surface properties that adjust in response to external cues. The control of the surface properties combined with the plasmonic signal enhancement through the NP core renders L-NPs bright Raman tags for the identification of biomarker overexpression at the single-cell level.

Author contributions: X.A., A.M., J.K.S., J.E.S., and B.M.R. designed research; X.A., A.M., J.M., J.Y., T.P., Z.H., T.L., and J.E.S. performed research; J.Y., T.P., Z.H., T.L., and J.K.S. contributed new reagents/analytic tools; X.A., A.M., J.M., and B.M.R. analyzed data; and X.A. and B.M.R. wrote the paper.

The authors declare no competing interest.

This article is a PNAS Direct Submission.

[1]To whom correspondence may be addressed. Email: bmr@bu.edu.

This article contains supporting information online at https://www.pnas.org/lookup/suppl/doi:10.1073/pnas.2105913118/-/DCSupplemental.

Published August 13, 2021.

elucidate the underlying mechanisms that determine the orientation of the tags in the membrane, and utilize them to engineer plasmon-enhanced Raman probes for the detection of epidermal growth factor receptor (EGFR)-overexpressing cancer cells.

Results

Synthesis of Modified Tags and Incorporation into NP-Supported Membranes. Three tag molecules were synthesized and characterized in this study: cholesteryl hexynoate (Tag-1), cholesterol succinoylpropargyl amide (Tag-2), and betulin 28-succinoylpropargyl amide (Tag-3) (Fig. 1*A*). The tags were prepared following established procedures (35) or by applying routine synthesis protocols (*SI Appendix*, Fig. S1) and characterized by ^{1}H– and ^{13}C–nuclear magnetic resonance, as well as high-resolution mass spectrometry (HRMS) (*SI Appendix*). The tags retain the lipophilic terpenoid ring structure, which allows them to integrate into lipid membranes and stabilize lipid organization and packing, as is known from unmodified sterols. The hydroxyl group on cholesterol C3 or betulin C28 (Fig. 1*A*, red arrows) are derivatized to introduce side chains of different lengths and polarity as well as a terminal alkyne group. Compared to Tag-1, the modified side chains for Tag-2 and Tag-3 are longer and contain an additional amide group that increases the polarity and the number of hydrogen bond donors/acceptors in the side chain. The partial charge distribution in the modified side chains is illustrated by Hirshfeld charge analyses (36), performed for all tags under lipid membrane-mimicking conditions with a dielectric constant $\varepsilon = 2$ (Fig. 1*A*). Similar charge distributions are obtained in the gas phase or with an implicit solvation of water (*SI Appendix*, Fig. S2).

Tag-1 to Tag-3 were incorporated into the lipid membrane of an L-NP architecture in a modified one-pot self-assembly approach, as reported previously (4, 7). In this work, 40 nm Ag NP cores and a lipid composition of 55 mol% zwitterionic 1,2-dipalmitoyl-sn-glycero-3-phosphocholine (DPPC), 5 mol% anionic 1,2-dioleoyl-sn-glycero-3-phospho-L-serine (DOPS), and 40 mol% of one of the three tag species were used unless otherwise noted. This assembly approach generates a hybrid membrane that contains an outer lipid monolayer tethered through hydrophobic interactions to an inner octadecanethiol (ODT) layer, which is covalently bound to the metal NP surfaces (Fig. 1*B*) (5, 16, 17). The hybrid membrane shares similarities with bilayer membrane models, although it could show a different level of membrane order than ideal bilayers. Successful lipid membrane formation in L-NPs was demonstrated using fluorescently labeled lipids through optical colocalization of fluorescent membrane signal and NP scattering signal in correlated fluorescence (FL) and darkfield (DF) imaging of surface-immobilized L-NPs. For all modified tags, a strong spatial correlation of the DF signal from the metal core and the FL signal from the membrane layer was observed (*SI Appendix*, Fig. S3). The average hydrodynamic diameters of the nanocomposites were measured to be 56.7 ± 4.8 nm for Tag-1–containing L-NPs (L-NP–Tag-1), 53.4 ± 3.4 nm (L-NP–Tag-2), and 59.7 ± 2.7 nm (L-NP–Tag-3). These diameters are similar to that of a control group with unmodified cholesterol (L-NP–Chol) (*SI Appendix*, Table S1).

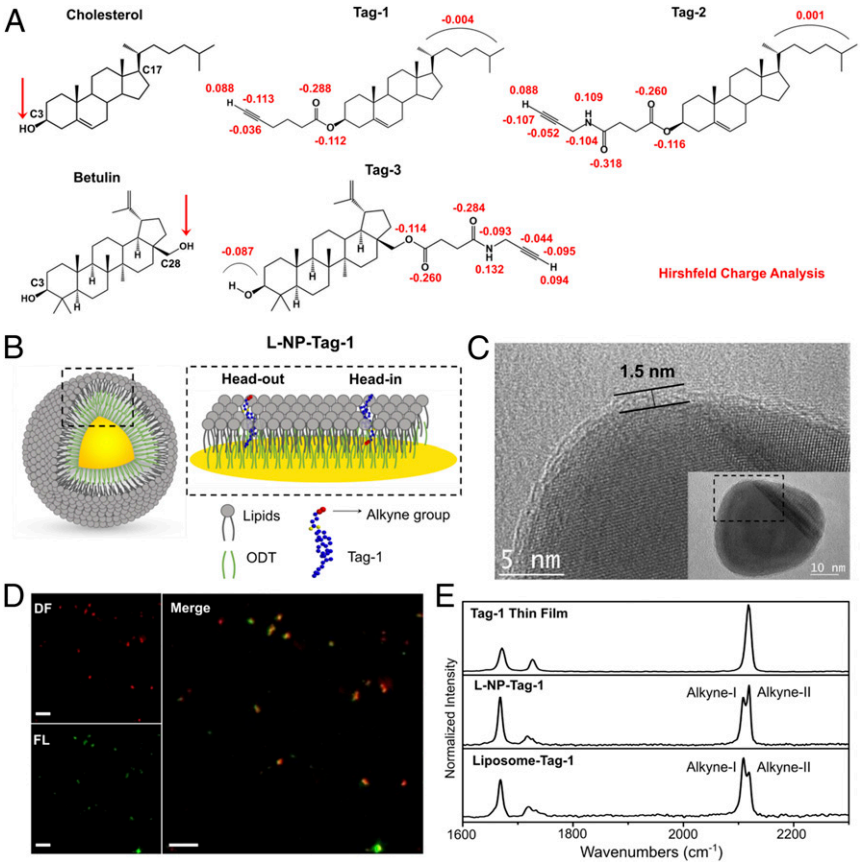

Fig. 1. Molecular structures of Tag-1 to Tag-3 and characterization of L-NP–Tag-1. (*A*) Molecular structures of cholesterol, betulin, and alkyne-modified Tag-1 to Tag-3, with Hirshfeld partial charge calculations. (*B*) Scheme of L-NP–Tag-1. (*C*) TEM micrographs of L-NP–Tag-1. (*Inset*) A zoom-out view of imaged nanocomposite, with the zoomed-in area indicated by the dashed rectangle. (*D*) Correlated DF (*Top Left*), FL (*Bottom Left*) images, and a channel merge (*Right*) of L-NP–Tag-1 after the fluorescent click assay. (Scale bars, 10 μm.) (*E*) Raman spectra of Tag-1 (*Top*), L-NP–Tag-1 (*Middle*), and liposome–Tag-1 (*Bottom*).

Transmission electron microscopy (TEM) micrographs of L-NP–Tag-1 show a uniform lipid membrane around the NP core (Fig. 1*C*). The average thickness of the membranes in the TEM images is 2.2 ± 0.4 nm, nearly identical to that of L-NP–Chol (2.3 ± 0.4 nm). This membrane thickness is smaller than what would be expected based on a simple addition of the thicknesses of a DPPC monolayer (16.1 Å) (37) and an ODT layer (16.0 Å) (38), and is consistent with a hybrid membrane structure that lacks an interstitial space between ODT and lipid layer and, instead, contains the outer lipid monolayer interdigitated in the inner ODT layer (4, 5, 39).

Characterization of L-NP–Tag-1. To probe the availability of alkyne groups on the surface of L-NP–Tag-1, a fluorescent click assay was performed that conjugates alkyne groups with fluorescent azide molecules (*SI Appendix*, Fig. S4 and *Materials and Methods*) (40). After the click reaction, correlated DF/FL imaging on L-NP–Tag-1 colloids reveals a strong spatial correlation of DF and FL signals (Fig. 1*D*) with high Manders colocalization coefficients (41), M_1 (correlation of DF signals with FL) = 0.83 ± 0.14 and M_2 (correlation of FL with DF) = 0.85 ± 0.07. Control L-NPs containing unmodified cholesterol (L-NP–Chol) do not show appreciable FL signals with the same protocol (*SI Appendix*, Fig. S5*A*) (M_1 = 0.01 ± 0.01 and M_2 = 0.25 ± 0.32). Overall, these data confirm the presence of solvent-accessible terminal alkyne groups in L-NP–Tag-1 that facilitate a successful click conjugation.

Next, Raman spectra were recorded for drop-casted thin films of Tag-1, L-NP–Tag-1, and a liposome–Tag-1 control with conventional lipid bilayers. The liposomes were assembled from the same lipid composition used for L-NP–Tag-1. The average width of the lipid bilayer membrane in the liposome controls was determined from TEM images as 6.1 ± 1.0 nm (*SI Appendix*, Fig. S5 *B* and *C*). As shown in Fig. 1 *E*, *Top* and *SI Appendix*, Fig. S6*A*, the spectrum of the Tag-1 thin film shows a sharp, distinct peak at 2,118.4 ± 1.0 cm^{-1} with a narrow full width at half maximum (FWHM) of 9.9 ± 1.3 cm^{-1}, which can be assigned to the alkyne-stretching mode. In addition, a distinct C = C-stretching mode at 1,667.8 ± 0.9 cm^{-1} as well as a carbonyl-stretching band at 1,717.1 ± 1.1 cm^{-1} are also detected. Intriguingly, different from the Tag-1 thin film, the alkyne-stretching bands of L-NP–Tag-1 (Fig. 1 *E*, *Middle*) and liposome–Tag-1 (Fig. 1 *E*, *Bottom*) are split into a doublet shape with two distinct peaks. For L-NP–Tag-1, the two peaks lie at 2,108.8 ± 0.8 cm^{-1} and 2,118.6 ± 0.8 cm^{-1}, with FWHMs of 9.5 ± 1.2 cm^{-1} and 10.3 ± 1.4 cm^{-1}, as determined by Lorentzian fits. These two peaks are referred to as alkyne I and alkyne II, respectively, throughout this manuscript. An ensemble-averaged SERS enhancement factor of 3.9×10^4 is calculated for L-NP–Tag-1 based on the alkyne II peak intensity with 532-nm excitation. Raman spectra of aqueous suspensions of L-NP–Tag-1 were also recorded (*SI Appendix*, Fig. S6*B*) and were found to exhibit an identical doublet peak shape for the alkyne-stretching band with peak maxima at 2,108.8 ± 0.8 and 2,119.9 ± 0.7 cm^{-1}.

Similar doublet peak shapes, as shown with L-NP–Tag-1, were also observed for other types of lipid-coated, Tag-1–incorporating control nanocomposites, prepared with cores of different sizes, shapes, and compositions (Fig. 2 and *SI Appendix*, Fig. S7). Nanocomposites containing Au NPs (20, 40, and 80 nm), Ag NPs (40 and 80 nm), Au nanorods, SiO_2@Au core–shell NPs, mesoporous SiO_2 NPs, or polylactic acid (PLA) NPs as cores were found to exhibit similar spectral features in the alkyne-stretching region as L-NP–Tag-1, which suggests that the splitting of the alkyne-stretching peak is general in Tag-1–containing, NP-supported lipid membrane architectures.

Raman spectroscopy provides detailed structural information and can resolve molecular orientations in membranes (42, 43); one possible explanation for the observed splitting of the alkyne-stretching band in L-NP–Tag-1 is the coexistence of two distinct orientations of the Tag-1 molecule in the membrane. Previous studies on unmodified cholesterol have shown that three orientational modes can exist in lipid bilayer membranes: a canonical orientation in which the sterol lies parallel to the lipid molecules and the cholesterol hydroxyl group is positioned between the lipid head groups, an inverse orientation in which the hydroxyl group is embedded in the lipid tails of the surrounding lipids, and a "horizontal" orientation in which the sterol lies in the interstice between the two lipid leaflets of a lipid membrane, with an orientation perpendicular to the lipid molecules (44–47). A coexistence of different orientations is likely to occur in membranes with high levels of unsaturated lipids (45, 47) or when the sterol hydroxyl is substituted with less polar functional groups (48, 49). Based on these previous findings, we tentatively attribute the doublet in the alkyne-stretching region of the L-NP–Tag-1 spectra to a coexistence of two orientations: a "head-out" orientation corresponding to the canonical mode of unmodified cholesterol, in which the terminal alkyne group of the modified tag points toward the lipid–water interface and a "head-in" orientation that contains the alkyne pointing toward the metal core, corresponding to the inverse mode (Fig. 1 *B*, *Right*). Because of an absence of an interstitial space in the interdigitated lipid–ODT hybrid membrane architecture, significant contributions from the horizontal orientation can be excluded for L-NPs.

Coexistence of Head-in and Head-out Orientations of Tag-1 in L-NP–Tag-1. To assign the alkyne I and alkyne II modes to a particular orientation in the membrane, we first measured the alkyne-stretching frequencies of Tag-1 dissolved in solvents with different polarities (50), including ethanol, acetone, and chloroform (Fig. 3*A*). These spectra provide an experimental measure for the magnitude of the spectral shift in the alkyne-stretching frequency in dielectric environments that mimic lipid head groups or tails. The alkyne-stretching band of Tag-1 gives rise to a single, symmetric peak in all solvents that shifts toward higher wavenumbers as the polarity of the solvent decreases. When the solvent is changed from the more polar solvent ethanol to the relatively nonpolar solvent chloroform, the peak positions of the alkyne-stretching peak shifts from 2,109.1 ± 2.1 cm^{-1} to 2,118.5 ± 0.5 cm^{-1}. These peak positions are essentially identical to those determined for alkyne I (2,108.8 ± 0.8 cm^{-1}) and alkyne II (2,118.6 ± 0.8 cm^{-1}) in L-NP–Tag-1. The same experiment was also performed with Tag-3, for which a similar trend is observed (*SI Appendix*, Fig. S6*C*).

The Raman spectra of Tag-1 were also calculated through BP86/DEF2-SV(P)/D3BJ calculations (*SI Appendix*) in 1) the gas phase; 2) a conductor-like polarizable continuum model (CPCM) with a dielectric constant ε = 2, mimicking the hydrophobic condition of lipid tails; and 3) a CPCM model of water (Fig. 3*B*). The calculations predict alkyne-stretching peaks for Tag-1 at 2,118 cm^{-1} in the gas phase, 2,111 cm^{-1} in the dielectric medium with ε = 2, and 2,105 cm^{-1} in water. Both the experimental and calculated relationship between the alkyne-stretching mode peak position and the dielectric environment are consistent with an assignment of the alkyne I peak to the head-out orientation (sampling the aqueous medium) of Tag-1 and the alkyne II peak to the head-in orientation (sampling the lipid tails of the membrane). Additional evidence supporting this peak assignment stems from control experiments, in which liposomes were produced with unmodified cholesterol and alkyne-conjugated lipids that contain an alkyne group either in the lipid head group [(i) hexynoyl PE, Fig. 3 *C*, *Top*] or in the tail [(ii) 16:0(alkyne)–18:1 PE, Fig. 3 *C*, *Bottom*]. The Raman spectra measured for the two different controls show significant differences in the spectral position of the alkyne-stretching mode. The spectrum of (i) exhibits an alkyne-stretching peak at 2,112 ± 1.2 cm^{-1}, which is similar to the alkyne I peak observed for L-NP–Tag-1 (Fig. 3*D*). The spectrum of (ii) contains an alkyne-stretching peak at 2,119.5 ± 2.1 cm^{-1}, close to the alkyne II peak of L-NP–Tag-1. The spectra of the modified lipids confirm that the stretching mode of the alkyne

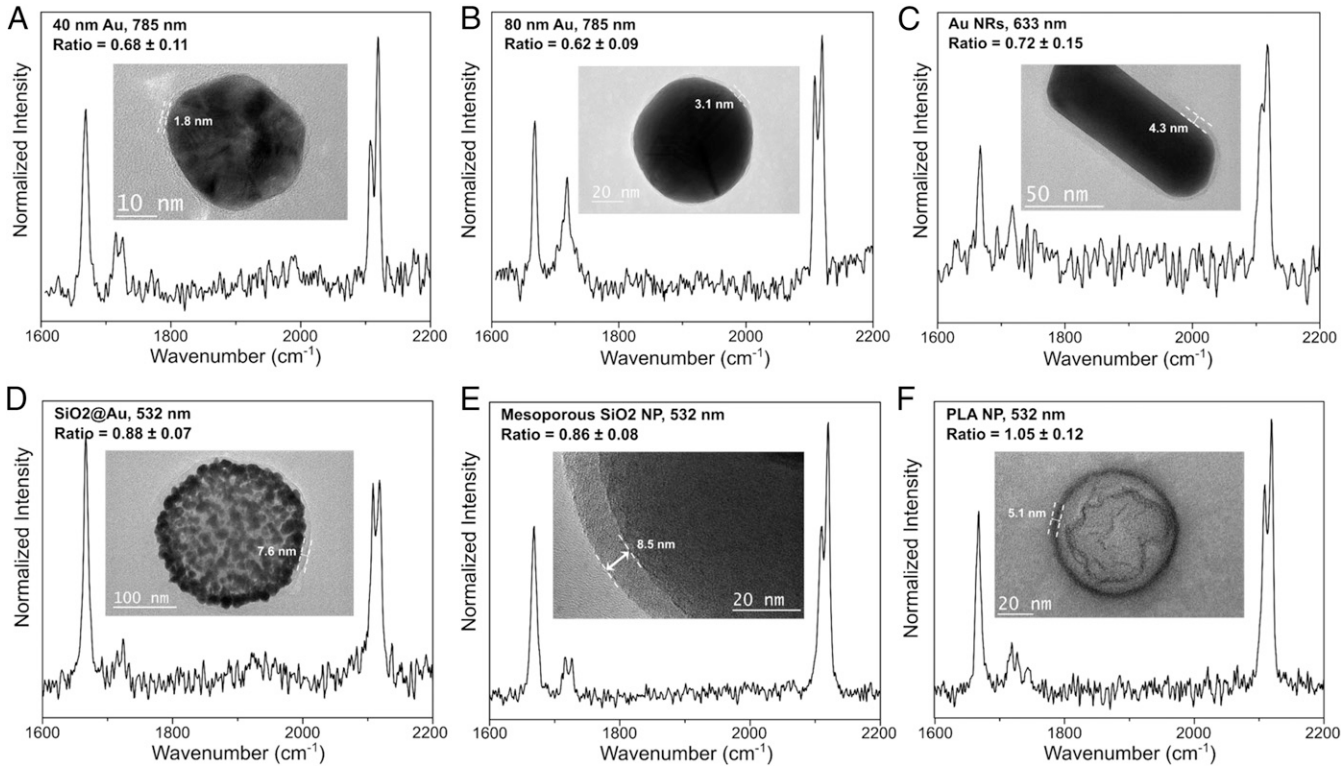

Fig. 2. Characterization of different Tag-1–incorporating nanocomposites. (*A–F*) Raman spectra and TEM micrographs of lipid-wrapped, Tag-1–incorporating nanocomposites with 40 nm Au NPs (*A*), 80 nm Au NPs (*B*), Au nanorods (NRs) (*C*), SiO_2@Au core–shell NPs (*D*), mesoporous SiO_2 NPs (*E*), and PLA NPs (*F*), as cores at indicated excitation wavelengths. Alkyne I/alkyne II–integrated intensity ratios are calculated by peak areas from Lorentzian peak fits from 10 spectra obtained in three independent experiments (*SI Appendix*).

groups shifts to higher wavenumbers when localized in the hydrophobic region of the membrane.

The resonant SERS signal amplification scales with the fourth power of the E-field, which decreases as the separation from the NP surface increases (11, 12, 51). Because of this distance dependence, even relatively small changes in separation between a Raman-active group and the NP surface can result in significant differences in the recorded Raman signal. The difference in the distance between the alkyne group and the metal surface for the head-out and head-in orientations of Tag-1 is estimated to be >1.5 nm (44). Consequently, we expect the alkyne-stretching mode associated with the head-in orientation (alkyne II), whose alkyne group is located closer to the metal NP, to experience, on average, a stronger signal amplification under resonant excitation than the alkyne I mode associated with the head-out orientation. To test this hypothesis, the integrated intensity ratios of the alkyne I to alkyne II bands at three different excitation wavelengths (532, 633, and 785 nm) for L-NP–Tag-1, liposome–Tag-1, as well as an L-NP_{Au}–Tag-1 control were calculated from the fitted peak areas (*SI Appendix*). The latter was prepared with the identical lipid membrane as L-NP–Tag-1 but using a 40 nm Au NP core instead of Ag NP. The plasmon resonance maxima of L-NP–Tag-1 and L-NP_{Au}–Tag-1 thin films were measured to be around 550 and 750 nm, respectively (*SI Appendix*, Fig. S6 *D* and *E*). All three investigated groups exhibit a distinct doublet shape in the alkyne-stretching region. For liposome–Tag-1 that lacks a metal NP core, the alkyne I/alkyne II Raman intensity ratios (Fig. 3*E*) show no noticeable difference between the three excitation wavelengths. Intensity ratios close to 1 for all wavelengths indicate that, during the formation of the lipid membranes, head-out and head-in orientations are equally favored in the lipid layer. Importantly, for both L-NP–Tag-1 and L-NP_{Au}–Tag-1, the alkyne I/alkyne II ratio drops significantly when the excitation wavelength overlaps with the plasmon resonance of the drop-coated L-NP films (i.e., at 532 nm with L-NP–Tag-1 and 785 nm with L-NP_{Au}–Tag-1) (Fig. 3*E*). The 633-nm excitation overlaps weakly with the broad plasmon spectra of both Ag and Au L-NPs, and the integrated peak intensity ratios are decreased relative to the "off-resonance" conditions (785 nm for silver and 532 nm for gold, $P = 0.01$) but not as much as for the "on-resonance" conditions. Notably, in both L-NP–Tag-1 and L-NP_{Au}–Tag-1, alkyne I/alkyne II intensity ratios of around 0.7 for on-resonance conditions are consistent with a 1.5- to 2-fold lower SERS signal enhancement for alkyne I compared to alkyne II, predicted by the distance dependence of the E-field intensity around individual Au NPs in a Au NP film (52). The observed differences in the alkyne I/alkyne II intensity ratio as a function of excitation wavelength confirms that the alkyne II peak intensity experiences a stronger enhancement than the alkyne I peak intensity under resonant excitation, which corroborates our assignment of the alkyne II peak to the Tag-1 head-in orientation and of the alkyne I peak to the head-out orientation.

The head-out orientation of Tag-1 presents the terminal alkyne at the lipid–solution interface, in which it can react with azides in solution through click chemistry to form a triazole product (40), while the head-in orientation is protected by the lipid layer and not readily accessible for chemical reactions. After click reaction of L-NP–Tag-1 with azides, the Raman spectra contain a new peak in the C = C-stretching range at 1,644.2 ± 2.7 cm^{-1} (Fig. 3*F*, red arrow), which confirms the formation of the triazole product (53). After normalization with the lipid -CH_2- symmetric stretching band at 2,850 cm^{-1} as internal standard (54), the alkyne I peak exhibits a significant decrease in intensity, whereas the alkyne II peak intensity remains almost unchanged (Fig. 3 *F*, *Inset*), which further confirms our orientation assignment. Overall, the

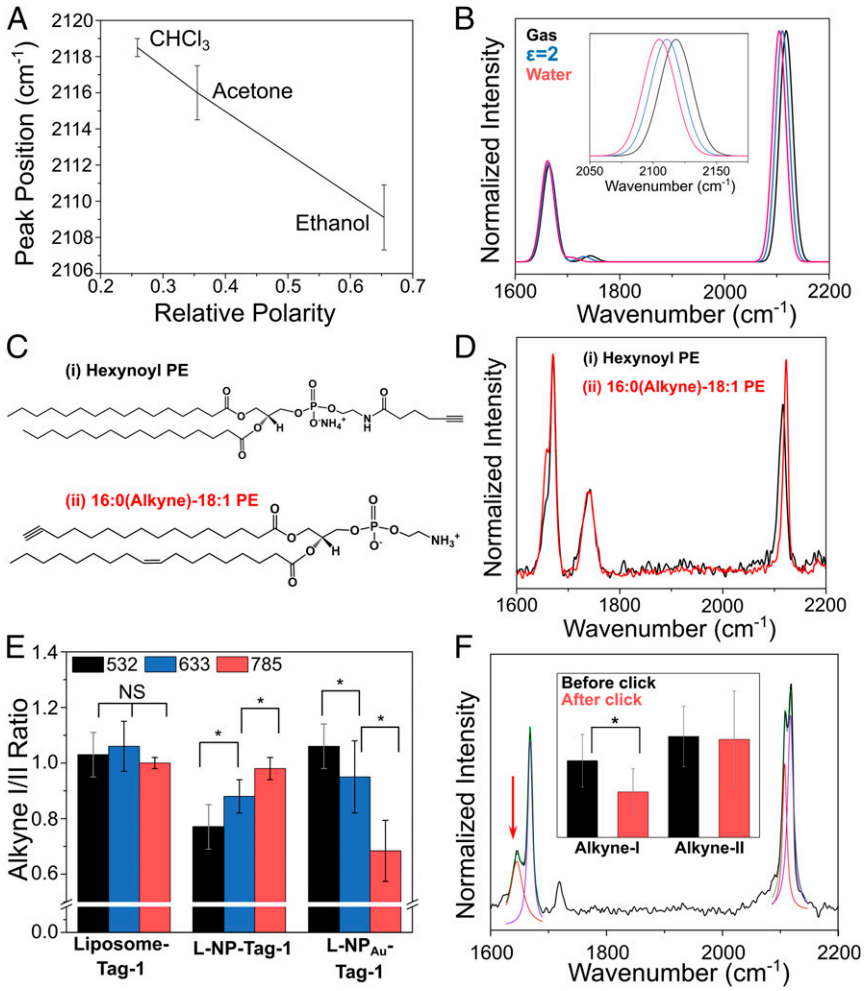

Fig. 3. Evidence for Tag-1 orientation in lipid membranes. (*A*) Plot of the alkyne-stretching frequencies of Tag-1 dissolved in different solvents versus relative solvent polarity. (*B*) BP86/DEF2-SV(P)/D3BJ[/CPCM(H_2O/ε = 2)] calculations of Raman vibrational frequencies of Tag-1 alkyne-stretching peak in gas phase (black), in a lipid membrane mimic with ε = 2 (blue), and with a CPCM-implicit solvation of water (red). (*Inset*) Zoom-in on the alkyne-stretching peak frequencies. (*C* and *D*) Molecular structures (*C*) of hexynoyl PE [1,2-dipalmitoyl-sn-glycero-3-phosphoethanolamine-*N*-(5-hexynoyl)] (*Top*) and 16:0(alkyne)-18:1 PE (1-hexdec-15-ynoyl-2-oleoyl-sn-glycero-3-phosphoethanolamine) (*Bottom*) and Raman spectra of liposome containing the two lipids (*D*). (*E*) Alkyne I/alkyne II–integrated intensity ratios with different excitation wavelengths for liposome–Tag-1, L-NP–Tag-1, and L-NP_{Au}–Tag-1; *: significant difference at $P = 0.01$; NS: nonsignificant difference at $P = 0.5$. (*F*) Raman spectrum and Lorentzian fits of L-NP–Tag-1 after click conjugation of azide-PEG-biotin; (*Inset*) integrated peak intensity ratios of alkynes I or II to lipid -CH_2– stretching internal standard before (black) or after (red) click reaction. Error bars: Mean ± SD from 30 spectra from three independent measurements.

experimental data point toward a coexistence of the head-in and head-out orientations as the most likely cause of the observed doublet shape in the alkyne-stretching region for L-NP–Tag-1.

Disruption of the Interfacial Lipid–Water Hydrogen-Bonding Network Determines the Orientation of Tag-1. To acquire further information on the stability and thermodynamics of the two distinct Tag-1 orientations, we investigated the integrated intensity ratios of alkyne I and alkyne II in the Raman spectra of L-NP–Tag-1 as a function of temperature. A water suspension of L-NP–Tag-1 colloid was used in these experiments, and Raman spectra were continuously measured while the temperature was increased in situ from room temperature (RT) to 65 °C. Intriguingly, the alkyne I peak intensity as well as the alkyne I/II intensity ratio gradually decrease as the temperature increases (Fig. 4*A*). At 63.7 °C and above, only a single alkyne-stretching peak remains at 2,118.7 ± 0.4 cm^{-1}, which is essentially identical to the alkyne II peak (head-in mode) prior to heating (2,118.6 ± 0.8 cm^{-1}). Examination of the alkyne II peak intensity normalized by the lipid internal standard reveals a significant increase after heating (*SI Appendix*, Fig. S8*A*). After the colloid was cooled down to RT, the L-NP–Tag-1 alkyne-stretching band contained only a single, symmetric peak close to the alkyne II peak position (2,109.1 cm^{-1}, *SI Appendix*, Fig. S8 *B* and *C*). No significant changes in the morphology of the membrane or leaching of Tag-1 from L-NP–Tag-1 were observed after heating (*SI Appendix*, Fig. S8 *A* and *D*). Overall, these observations suggest that heating induces an irreversible reorientation of Tag-1 in the lipid membrane from head out to head in. The orientational change of Tag-1 is further corroborated by the fluorescent click assay performed on L-NP–Tag-1 after heating. Correlated DF/FL imaging showed only weak FL signals with poor colocalization with DF signals (M_1 = 0.03 ± 0.05 and M_2 = 0.01 ± 0.01) (*SI Appendix*, Fig. S8*E*). The poor click conjugation efficiency confirms the prevalence of the head-in orientation, which localizes the alkyne group in a solvent-inaccessible environment and prevents a successful conjugation after heating.

What are the driving forces for the heat-induced reorientation of Tag-1 in NP-supported lipid membranes? The zwitterionic lipids in L-NPs can form an extensive hydrogen-bonding network (HBN) at the membrane/water interface with interfacial water

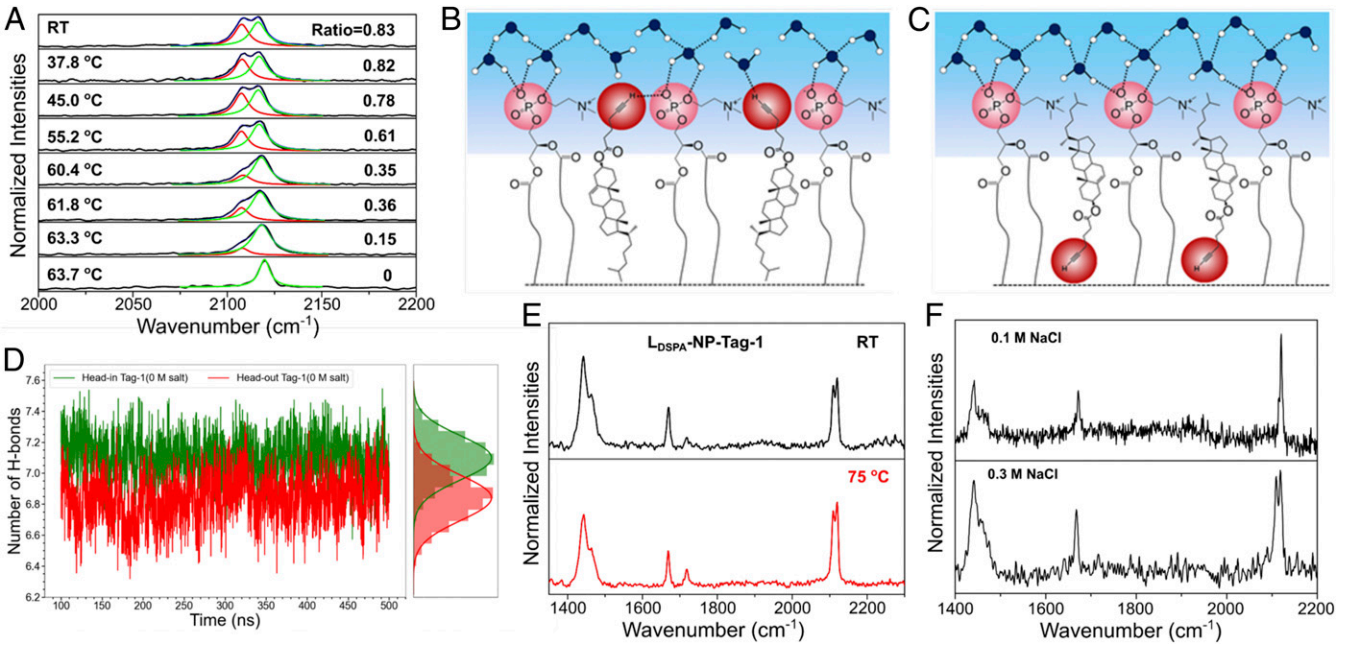

Fig. 4. Characterization of thermal-induced orientation change of Tag-1 in L-NP–Tag-1. (*A*) Raman spectra and Lorentzian peak fits of the alkyne-stretching bands of L-NP–Tag-1 colloid suspension under in situ heating to different temperatures. (*B* and *C*) Graphical representations of the HBN between DPPC head group and interfacial water molecules with head-out (*B*) or head-in (*C*) orientation of Tag-1. (*D*) Instantaneous average number of hydrogen bonds formed between a single DPPC lipid and interfacial water molecules for a lipid membrane containing Tag-1 head-in (green) or head-out (red) orientations. (*E*) Raman spectra of L_{DSPA}-NP–Tag-1 control composite before and after heating to 75 °C for 30 min. (*F*) Raman spectra of L-NP–Tag-1 after heating to 75 °C for 30 min in 0.1 M (*Top*) or 0.3 M (*Bottom*) NaCl.

molecules located in the immediate vicinity of the lipid head groups (55–57). Prior sum–frequency generation spectroscopy studies have shown that the strong HBN at the lipid membrane/water interface effectively repels solutes that would perturb and weaken the HBN (56, 57). These hydration phenomena are considered a key factor in the anti-fouling properties of lipid membranes and can be expected to impact the orientation of Tag-1 in L-NP membrane as well. The modified side chain introduced at the cholesterol C3 in Tag-1 positions the alkyne group into the plane containing the lipid head groups (see atom numbering in Fig. 1*A* and *SI Appendix*, Fig. S9), in which it can form weak hydrogen bonds with water or lipid molecules (Fig. 4*B* and *SI Appendix*, Fig. S10*A*). In contrast, the nonpolar carbon chain in position C17 does not engage in hydrogen bond formation when it is located in the same plane; as such, it does not impact the strong interfacial water–lipid HBN (Fig. 4*C*). Consequently, the interfacial HBN is more strongly restructured and perturbed for the head-out orientation of Tag-1 than for head in.

To substantiate this hypothesis, we performed all-atomic molecular dynamic (MD) simulations of the Tag-1 embedded in a lipid bilayer membrane model and characterized the HBN by calculating the number of hydrogen bonds formed between the zwitterionic head group of DPPC and water with Tag-1 in head-in and head-out orientation (Fig. 4*D*). These calculations reveal that a larger number of hydrogen bonds are formed between DPPC and interfacial water molecules when Tag-1 is in the head-in orientation (7.1 hydrogen bonds per DPPC molecule), as opposed to head out (6.8 per DPPC). This observation confirms that Tag-1 has a stronger disruptive effect on the lipid–water HBN in the head-out orientation. Considering the change in Gibbs free energy associated with the formation of hydrogen bonds between zwitterionic lipids and interfacial waters around −12 kJ/mol at RT, as previously reported (58), and a typical lipid-grafting density of one lipid molecule per 40 $Å^2$ on L-NP surfaces (2, 59), maximization of the HBN achieved by the conversion of head-out to head-in orientation represents a thermodynamic driving force of -4.15×10^{-17} J per particle (see *SI Appendix* for calculations). The high computed values of the liquid crystal order parameter for a lipid bilayer with identical compositions (*SI Appendix*, Fig. S10*B*) suggests that the hybrid membrane considered here is in a liquid-ordered phase at RT (29). Under these conditions, there is a substantial energy barrier for the flipping of Tag-1 from head-out to head-in orientation. The close packing of the lipids and the associated, high-activation energy barrier suppress the head-out to head-in transition at RT and effectively break the ergodicity of the system. However, at higher temperatures, the membrane undergoes a transition into a liquid-disordered phase, lowering the activation barrier for Tag-1 reorientation. The lower activation barrier and the higher available thermal energy facilitate the reorientation of Tag-1 into the preferred head-in orientation, minimizing the disruption of the HBN.

To experimentally test the role of the HBN in the Tag-1 reorientation, we evaluated the effect that the weakening of the HBN has on the relative stability of the head-in orientation. Weakening of the HBN can be achieved by replacing zwitterionic lipids in the membrane with lipids that carry a net charge (55, 56). For this purpose, L_{DSPA}-NP–Tag-1 were assembled, which contain the saturated, negatively charged lipid 1,2-distearoyl-sn-glycero-3-phosphate (DSPA) instead of the zwitterionic DPPC as the lipid skeletal component and that consequently resulted in nanocomposites with a much more negative ζ-potential than L-NP–Tag-1 (*SI Appendix*, Table S1). At RT, the alkyne-stretching band of L_{DSPA}-NP–Tag-1 shows a pronounced doublet shape with peak frequencies of 2,109.3 ± 0.4 cm^{-1} and 2,119.8 ± 0.4 cm^{-1}, similar to the alkyne I and II modes of L-NP–Tag-1. However, unlike in the case of L-NP–Tag-1, the doublet peak shape is retained for the alkyne-stretching band in L_{DSPA}-NP–Tag-1, even after heating to 75 °C for 30 min (Fig. 4*E*). An alternative strategy of weakening the HBN is based on increasing the electrolyte concentration in the aqueous medium around the L-NP–Tag-1 (55, 56). This is also captured by our MD studies, in which a higher salt concentration

results in a general decrease in hydrogen bond formation (*SI Appendix*, Fig. S10 *C* and *D*). When the salt concentration is increased from 0 M (as used in all previous experiments) to 0.1 M NaCl, heating of L-NP–Tag-1 to 75 °C for 30 min still induces a head-out to head-in transition in the alkyne-stretching frequencies of its Raman spectra, but the conversion is not complete, as an evident alkyne I feature still remains after heating (Fig. 4 *F*, *Top*). Importantly, when the salt concentration is further increased to 0.3 M NaCl, the conversion of the doublet alkyne peak shape into a single peak under heating is no longer observed (Fig. 4 *F*, *Bottom*). The increase in stability of the Tag-1 alkyne I feature at elevated temperatures in case of a weakened HBN provides experimental evidence that a strong HBN network is an essential factor for the heat-induced orientational changes in L-NP–Tag-1.

Characterizing Tag-2 and Tag-3 Orientations in NP-Supported Lipid Membranes. The predominance of the head-in orientation in L-NP–Tag-1 at higher temperatures due to interactions of Tag-1 with the HBN suggests that size and structure of the side chain present degrees of freedom to control the preferential orientation of the tag molecules in the membrane. To test this possibility, we included side chains with an overall increased polarity and a larger number of charge centers for increased hydrogen bonding with the water network in the designs of Tag-2 and Tag-3 (Fig. 1*A*). Intriguingly, the Raman spectra at RT for both Tag-2 and Tag-3 (*SI Appendix*, Fig. S11*A*) as well as L-NP–Tag-2 and Tag-3 (Fig. 5*A*) contain a single, well-defined alkyne-stretching peak. Peak-stretching frequencies of 2,131.4 ± 1.9 cm^{-1} (L-NP–Tag-2) and 2,124.0 ± 1.6 cm^{-1} (L-NP–Tag-3) were respectively observed, which is indicative of one dominating orientation of the tags in the membrane.

To determine the preferential tag orientation, we probed the solvent-accessible alkyne concentration on the nanocomposites using the fluorescent click assay. Strong spatial correlation of DF and FL signals (*SI Appendix*, Fig. S11 *B* and *C*), with high Manders colocalization coefficients (Fig. 5*B*) for L-NP–Tag-2 and L-NP–Tag-3, confirm a successful click conjugation. Furthermore, the Raman spectra of these nanocomposites show a measurable reduction in the normalized integrated peak intensity of the alkyne-stretching mode after the click reaction (Fig. 5*C*). These observations indicate that the alkyne groups in L-NP–Tag-2 and Tag-3 are accessible for chemical reactions at the lipid–water interface and imply a head-out orientation. Heating of L-NP–Tag-2 and L-NP–Tag-3 to 75 °C for 30 min did not affect the frequency of the alkyne-stretching peak or induce any new features in the alkyne-stretching region (Fig. 5*D*), and the fluorescent click assay performed after heating confirmed the solvent accessibility of the alkyne group (Fig. 5*B*). These data imply that the head-out orientation is preserved in L-NP–Tag-2 and Tag-3, even at higher temperatures. The difference in the preferential membrane orientation between Tag-1 (head in) and Tag-2 and Tag-3 (head out) confirm that side chains with overall higher polarity that can form a larger number of hydrogen bonds with the interfacial HBN succeed in stabilizing the tags in the head-out orientation.

Targeted Raman Imaging of EGFR-Overexpressing Cancer Cells with L-NP–Tag-1. Targeted Raman imaging of cancer cells using bright probes that recognize specific biomarkers is a promising strategy for detecting cancer at the single-cell level (33, 60, 61). L-NP–Tag-1 possess great potential as a probe for this purpose. The coexistence of head-out and head-in orientation of Tag-1 at RT provides the nanocomposite with both surface-accessible alkyne groups for the introduction of specific, targeting functionalities through chemical conjugation and protected alkyne groups that can sustain a characteristic, plasmon-enhanced spectral signature in Raman imaging. Here, we utilize the orientational dimorphism in L-NP–Tag-1 for the identification of epidermal growth factor receptor (EGFR)–overexpressing cancer cells through Raman imaging on the single-cell level. The alkynes in head-out orientation were clicked with azide-functionalized epidermal growth factor (EGF) to introduce an EGFR recognition element on the L-NP surfaces (L-NP–Tag-1–EGF). The nanoconjugates were then applied to two EGFR-overexpressing breast cancer cell lines, MDA-MB-468 (1.9×10^6 EGFR/cell) (62) and MDA-MB-231 (7.0×10^5 EGFR/cell) (63), as well as to HeLa cells with physiological EGFR expression levels (2.2×10^4 EGFR/cell) (64) as a negative control. An L-NP–Tag-1–EGF concentration of 100 pM, corresponding to an approximate tag concentration of 0.5 μM, was used in all cell experiments.

Scanning electron microscope (SEM) images of MDA-MB-468 and MDA-MB-231 cells incubated with L-NP–Tag-1–EGF, referred to as 468-NP and 231-NP in the following, show a high concentration of NPs on the cell surfaces (Fig. 6 *A* and *B*). In contrast, MDA-MB-468 incubated with L-NP–Tag-1 without EGF (468-control) show almost no NP binding (Fig. 6*C*), indicating that nonspecific binding is negligible. HeLa cells incubated with L-NP–Tag-1–EGF (HeLa-NP) showed a much lower NP-binding density (Fig. 6*D*) on the cell surface than observed for the 468-NP and 231-NP groups, which is expected because of the lower binding affinity of L-NP–Tag-1–EGF to HeLa than to EGFR overexpressors. The preferential binding of L-NP–Tag-1–EGF to MDA-MB-468 was further validated by energy dispersive X-ray spectroscopy element mapping of Ag on the cell surface (*SI Appendix*, Fig. S12). We also clicked EGF to liposome–Tag-1 to generate control Raman probes without SERS signal amplification and bound these liposomes to MDA-MB-468 cells (468-liposome) under identical conditions as for L-NP–Tag-1–EGF. Successful binding in this case was confirmed by correlated DF/FL images of the cells with fluorescently labeled liposome–Tag-1–EGF (*SI Appendix*, Fig. S13*A*).

The Raman spectra of individual cells of the 468-NP and 231-NP groups provide sufficient signal to noise for the detection of a single, alkyne-stretching peak at around 2,119.3 cm^{-1} (indicated by red arrows in Fig. 6 *E* and *F*) that originates from the alkyne II–stretching mode of Tag-1 in head-in orientation. The predominance of the alkyne II peak is consistent with a consumption of the head-out orientation (alkyne I) in the click conjugation of EGF. In contrast, neither the spectra of the 468-control (Fig. 6*G*) nor of HeLa-NP (Fig. 6*H*) contain any observable features in the alkyne-stretching frequency range. The specificity of the alkyne II signal of L-NP–Tag-1–EGF for EGFR-overexpressing cells makes it a useful marker for identifying EGFR overexpressors at the single-cell level through Raman imaging. To obtain Raman images, the spectra of single cells in the 468-NP or control groups were acquired with 1-μm step widths. The alkyne II–stretching mode at around 2,120 cm^{-1} of the L-NP–Tag-1–EGF nanocomposite was used as a "detection" channel; whereas 2,200 cm^{-1}, which is void of any specific Raman features, was used as a "blank" channel. For the 468-NP group, high-signal intensities in the detection channel (Fig. 6*I*, see also *SI Appendix*, Fig. S14) were observed across the entire mapped cell area (Fig. 6 *E*, *Inset*), consistent with a successful labeling with the nanocomposite Raman probes. Only very low-signal intensities were observed in the blank channel (Fig. 6*M*). Similar observations in both channels were made for 231-NP (Fig. 6 *J* and *N*). However, in the case of both 468-control and HeLa-NP, no significant signal intensity was detected in either detection or blank channel (Fig. 6 *K*, *L*, *O*, and *P*). The negligible alkyne II signal in these cases is consistent with a low, expected nanocomposite binding for these groups.

In the case of 468-liposome, the alkyne-stretching signal intensity detected from the cells (*SI Appendix*, Fig. S13 *B* and *C*) was much lower than for 468-NP, despite having high binding levels of liposomes. We attribute the gain in Raman signal intensity for 468-NP to the electromagnetic enhancement of the alkyne signal through the metal NP in L-NP–Tag-1, which makes these NPs more effective probes than liposome–Tag-1.

Our Raman imaging experiments confirm that EGF-conjugated L-NP–Tag-1 facilitate the detection of EGFR-overexpressing

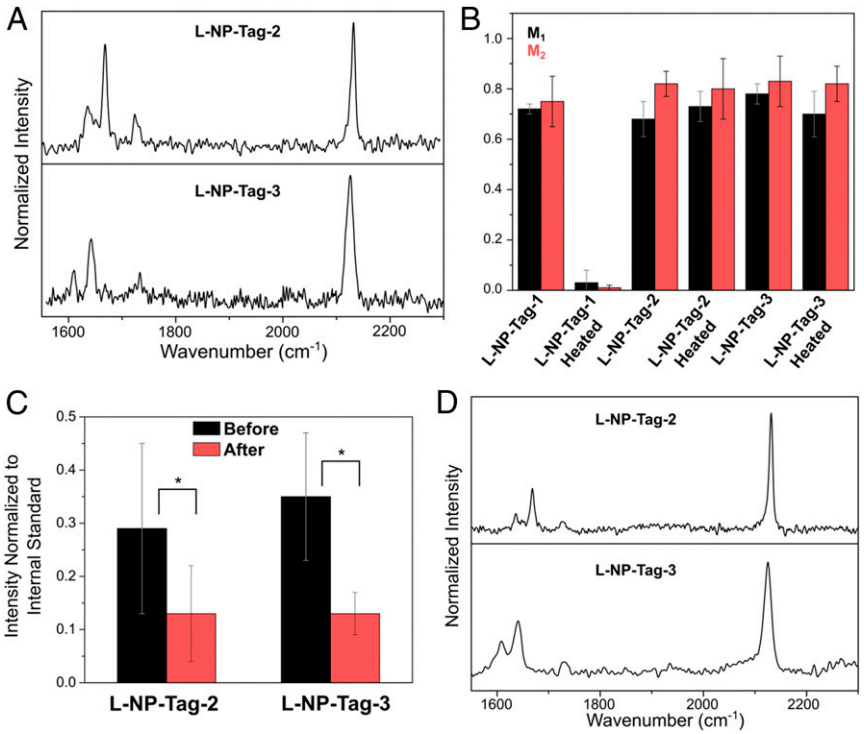

Fig. 5. Evidence for orientation of different tag molecules or nanocomposites. (*A*) Raman spectra of L-NP–Tag-2 (*Top*) and L-NP–Tag-3 (*Bottom*) drop coated on Si substrates. (*B*) Plot of Manders coefficients M_1 (correlation of DF with FL signals, black) and M_2 (correlation of FL with DF, red) after the fluorescent click assay for L-NP–Tag-1 to Tag-3 and L-NP–Tag-1 to Tag-3 after heating. Error bars: Mean ± SD from six sets of DF/FL images measured from three independent experiments. (*C*) Plot of the integrated peak intensity of the alkyne-stretching band of L-NP–Tag-2 and Tag-3 before (black) and after (red) click reaction, normalized to the lipid internal standard. Error bars: Mean ± SD from 10 spectra from three independent measurements. *, Significant difference at $P = 0.01$. (*D*) Raman spectra of L-NP–Tag-2 (*Top*) and L-NP–Tag-3 (*Bottom*) drop coated on Si substrates after heated to 75 °C for 30 min.

cancer cell lines at the single-cell level and their differentiation from cells with physiological expression levels.

Discussion

Modified sterols and terpenoid derivatives provide a facile, synthetic platform to control the surface properties of lipid–metal hybrid systems on molecular length scales. We have demonstrated in this work that the chemical modification of sterols or other terpenoid derivatives with side chains containing a terminal alkyne group can modulate their orientation in hybrid lipid membranes assembled around a metal NP core (L-NP) and thus directly affect the surface properties of L-NPs. The specific orientations of the investigated Tag-1 to Tag-3 probes were shown to depend on the structure and solvation properties of the modified chains. Tag-1 contains a side chain with a low number of hydrogen bond donors and acceptors that perturbs the HBN at the membrane/water interface. Under physiological conditions, Tag-1 shows a coexistence of head-in and head-out orientation in L-NP–Tag-1. At increased temperatures (>63.7 °C), Tag-1 molecules with head-out orientation can overcome the energetic barrier associated with a rotation in the membrane and convert into the head-in orientation to minimize the perturbation of the lipid–water HBN. The side chains introduced in Tag-2 and Tag-3 contain more polar charge centers than in Tag-1 and favor interfacial hydrogen bonding. Consequently, unlike Tag-1, Tag-2 and Tag-3 show a strong preference for the head-out orientation.

The coexistence of head-out and head-in orientations in L-NP–Tag-1 at RT provides functionalities for both chemical conjugation of a molecular, cell-binding ligand via the solvent-accessible terminal alkyne groups in the head-out orientation and plasmon-enhanced Raman imaging through "protected" alkyne groups with head-in orientation. This functional duality was utilized in this work to generate specific Raman labels with biorthogonal signals for the targeted Raman imaging of EGFR-overexpressing breast cancer cells, MDA-MB-468 and MDA-MB-231, and their distinction from cancer cells with physiological EGFR expression levels. The spatial resolution of ∼1 μm and integration times of 10 s for each pixel in our Raman-mapping experiments are comparable to previous spontaneous Raman cancer-mapping studies (61, 65, 66). L-NP–Tag-1 achieved sufficient contrast for single-cell detection with a tag concentration of 0.5 μM, which compares to 1 to 10 μM used in previous in vitro single-cell Raman-imaging studies with alkyne-based enhanced or nonenhanced Raman tags (61, 66, 67). L-NP–Tag-1 represents a promising diagnostic probe that enhances the sensitivity of cancer Raman imaging and enables cancer detection and identification at the single-cell level.

Although our study focused on nanocomposites with a 40 nm Ag NP core, we presented data that indicate that the coexistence of head-out and head-in orientations of Tag-1 is characteristic of a broad range of lipid-coated nanostructures with different core sizes, shapes, and compositions (Fig. 2), including metal or polymer cores. Modified sterols and terpenoids could, thus, provide a general strategy to modulate the surface chemical properties of lipid-coated NPs. The ability to control molecular orientation on the surface of L-NPs also has general relevance beyond the specific application as Raman tag in this study. Rationally designed sterols with configurable orientations are of interest not only for many sensing, diagnostic, and therapeutic strategies but also for applications such as smart sampling and plasmonic nanoreactors (4). It is conceivable that through the integration of multiple sterols that undergo orientational changes in response to defined external cues (e.g., temperature and irradiation) into L-NP platforms, the surface properties and, thus, the ability to interact with their environment can actively evolve to carry out different tasks

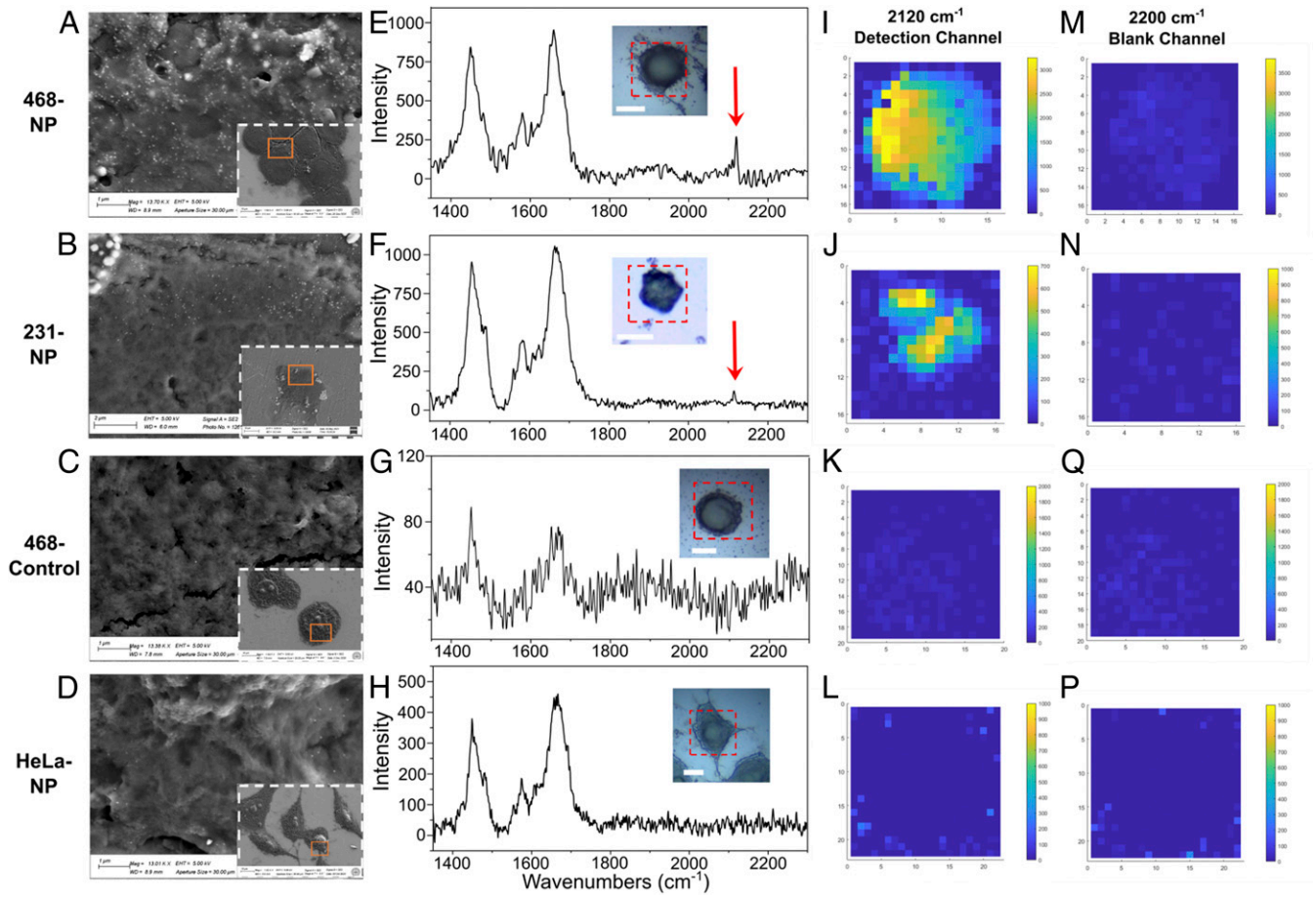

Fig. 6. Targeted Raman imaging of EGFR-overexpressing cancer cells and controls. (*Top row*) MDA-MB-468 cells incubated with 100 pM L-NP–Tag-1–EGF (468-NP); (*Second row*) MDA-MB-231 cells incubated with 100 pM L-NP–Tag-1–EGF (231-NP); (*Third row*) MDA-MB-468 cells incubated with 100 pM L-NP–Tag-1 (468-control); (*Bottom row*) HeLa cells incubated with 100 pM L-NP–Tag-1–EGF (HeLa-NP). (*A–D*) Scanning electron microscope images of cell surfaces. (*Insets*) Zoomed-out views of the imaged cells, with the zoomed-in area indicated by orange rectangles. (*E–H*) Raman spectra on EGFR-overexpressing cancer cells and controls. (*Insets*) Optical images of the mapped cells with the mapped area in dashed squares. (Scale bars, 10 μm.) (*I–P*) Raman maps generated from the detection channel at 2,120 cm^{-1} (*I–L*) and the blank channel at 2,200 cm^{-1} (*M–P*). The mean + SD of the spectra at 1,800 to 1,900 cm^{-1} is used as a threshold for generating the maps; pixels with signal intensities below the threshold are set to 0.

as a function of location and time. It is clear that the lipid coating in L-NPs is more than a biomimetic surface coating, as it provides a matrix for active surface control whose abilities remain to be fully explored in the future.

Materials and Methods

Preparation of L-NP–Tags. Chloroform solutions of 55 mol% DPPC (Avanti Polar Lipids), 5 mol% DOPS (Avanti Polar Lipids), and 40 mol% tags were mixed at a total amount of 1 μmol. The mixture was rotary evaporated at 32 °C to remove the chloroform, desiccated, and resuspended in water by tip sonication to form liposome–Tag suspensions. Afterward, an 80 μL 2 mg/mL ethanol solution of ODT (Sigma Aldrich) and a 1 mL colloid of 10^{10} particle/mL 40 nm Ag NP suspension (NanoComposix) were added into the liposome suspension. The mixture was shaken in dark at RT overnight before being centrifuged, washed with water, combined, and stored at 4 °C for later use.

MD Simulations of Tag-1 in Lipid Bilayer. The membrane lipid bilayer of composition 55% DPPC, 5% DOPS, and 40% Tag-1 with a total number of 200 lipid molecules was prepared using packmol package (68). Tag-1 molecule was simulated in both the head-in and head-out orientations. At RT, on the time scale of our simulations, no flipping of the Tag-1 molecule between the head-in and head-out orientations is observed. The all-atom model for Tag-1 molecule was prepared using the CGenFF module (69). DPPC and DOPS were simulated by using CHARMM36 lipid force field (70). Each lipid bilayer was solvated by 36 water molecules per lipid, defined by TIP3P water model (71). A K^+ and Cl^- ion concentration of 0.3 and 0 M, respectively, was used (10 K^+ was placed to neutralize the charges on DOPS). A minimum of 30-ns simulation was performed to equilibrate the bilayer system according to the CHARMM–GUI protocol (72). A leapfrog integration method with 2 fs time step was used for the NPT simulation. The pressure was maintained at 1 bar using semiisotropic Parrinello–Rahman barostat. A Nosé–Hoover thermostat was used to maintain the temperature of the simulation at 303 K. A 500-ns simulation was performed for all production run simulations. All the simulation was performed using GROMACS 2018.3 program (73).

Fluorescent Click Assay. Aliquoted reaction mixtures containing 30 μL water suspension of L-NP–Tags, 60 μL 10-mM azide-PEG_3-biotin (Sigma Aldrich) in 0.5× phosphate-buffered saline (PBS) buffer and 6 μL catalyst solution containing 1:1 (volume/volume) 0.005 M $Cu(II)SO_4{\cdot}5H_2O$ (Sigma Aldrich) and 0.05 M L-ascorbic acid (Sigma Aldrich) were prepared and kept at RT for 2 d before being dialyzed with nuclepore track-etched membranes (Whatman, pore size: 0.03 μm) in 0.1× PBS overnight. The dialyzed products were analyzed with Raman spectroscopy or further incubated with 1 mg/mL 0.5× PBS solution of the streptavidin Alexa Fluor 594 (Thermo Fisher Scientific) for correlated DF/FL imaging under an Olympus IX71 Inverted Microscope. Images were analyzed by ImageJ, and Manders coefficients were calculated with the JACoP ImageJ plugin (74).

Preparation of L-NP–Tag-1–EGF. Azide-functionalized EGF was first synthesized through acylation of primary amines. A total of 0.5 mL 1 mg/mL-1× PBS solution of EGF recombinant human protein (Thermo Fisher Scientific) was mixed with 3% (volume/volume) 0.44 M DMSO solution of azido-$dPEG_8$-NHS ester (Sigma Aldrich) and kept in ice bath for 6 h. Azide-functionalized EGF

product was then dialyzed with D-Tube dialyzers (Millipore) overnight to remove excessive azido-dPEG$_8$-NHS ester. Click reaction between L-NP–Tag-1 and azide-functionalized EGF was performed in reaction mixtures containing 50 μL L-NP–Tag-1 water suspensions, 50 μL azide-functionalized EGF, and 6 μL catalyst solution, as described in the *Fluorescent Click Assay* section. The click and subsequent dialysis procedures are identical to the previous section. For preparation of liposome–Tag-1–EGF, 50 μL liposome–Tag-1 water suspensions were used instead of L-NP–Tag-1, and all other steps are identical.

Raman Cell Imaging and Processing. Raman spectra and maps of cells were obtained with the Renishaw InVia Raman Microscope with 50× air objective (Leica, NA = 0.75), 532-nm excitation laser, and a diffraction grating of 2,400 l/mm. A combination of 1 μm step width, 10 s accumulation, and 270.4 μW laser power were used in the mapping experiments for each mapped pixel. Raman maps were generated on Matlab. A Savitzky–Golay filter was applied to smooth the data, and the signal intensity at the studied channel frequencies ± 5 cm^{-1} (2,115 to 2,125 cm^{-1} for detection channel and 2,195 to 2,205 cm^{-1} for blank channel) were integrated in each pixel. The mean + SD of the Raman signal intensity in each measured spectrum between 1,800 and 1,900 cm^{-1} is used as a threshold for that pixel in the generation of the map to preclude the contribution from the noise in the baseline; signals below the threshold are set to 0.

Data Availability. All study data are included in the article and/or *SI Appendix*.

ACKNOWLEDGMENTS. We thank the Chemical Instrumentation Center at Boston University for HRMS measurements. We thank Sara Mason and Jayraj Patel for help with tag syntheses and Han Zang for help with PLA NP synthesis. B.M.R. acknowledges support from the NIH through Grant R01CA138509. J.E.S. gratefully acknowledges the generous support of the NSF (Grant NSF CHE-1900416) and the NIH (Grant R01 GM107703-05).

1. X. Zhang, A. K. Pandiakumar, R. J. Hamers, C. J. Murphy, Quantification of lipid corona formation on colloidal nanoparticles from lipid vesicles. *Anal. Chem.* **90**, 14387–14394 (2018).
2. L. L. Olenick *et al.*, Lipid corona formation from nanoparticle interactions with bilayers. *Chem* **4**, 2709–2723 (2018).
3. J. A. Yang, C. J. Murphy, Evidence for patchy lipid layers on gold nanoparticle surfaces. *Langmuir* **28**, 5404–5416 (2012).
4. X. An, D. Stelter, T. Keyes, B. M. Reinhard, Plasmonic photocatalysis of urea oxidation and visible-light fuel cells. *Chem* **5**, 2228–2242 (2019).
5. Y. Guo, E. Terazzi, R. Seemann, J. B. Fleury, V. A. Baulin, Direct proof of spontaneous translocation of lipid-covered hydrophobic nanoparticles through a phospholipid bilayer. *Sci. Adv.* **2**, e1600261 (2016).
6. F. Xu *et al.*, Lipid-mediated targeting with membrane-wrapped nanoparticles in the presence of corona formation. *ACS Nano* **10**, 1189–1200 (2016).
7. X. Yu *et al.*, Glycosphingolipid-functionalized nanoparticles recapitulate CD169-dependent HIV-1 uptake and trafficking in dendritic cells. *Nat. Commun.* **5**, 4136 (2014).
8. F. Xu *et al.*, Membrane-wrapped nanoparticles probe divergent roles of GM3 and phosphatidylserine in lipid-mediated viral entry pathways. *Proc. Natl. Acad. Sci. U.S.A.* **115**, E9041–E9050 (2018).
9. X. Yu *et al.*, Dressing up nanoparticles: A membrane wrap to induce formation of the virological synapse. *ACS Nano* **9**, 4182–4192 (2015).
10. D. D. Lasic, D. Needham, The "stealth" liposome: A prototypical biomaterial. *Chem. Rev.* **95**, 2601–2628 (1995).
11. E. Hao, G. C. Schatz, Electromagnetic fields around silver nanoparticles and dimers. *J. Chem. Phys.* **120**, 357–366 (2004).
12. J. B. Jackson, N. J. Halas, Surface-enhanced Raman scattering on tunable plasmonic nanoparticle substrates. *Proc. Natl. Acad. Sci. U.S.A.* **101**, 17930–17935 (2004).
13. S. M. Bose, P. Longe, Plasmon structure in the x-ray absorption spectra of metals. *Phys. Rev. B* **18**, 3921 (1978).
14. S. T. Sivapalan *et al.*, Off-resonant two-photon absorption cross-section enhancement of an organic chromophore on gold nanorods. *J. Phys. Chem. Lett.* **4**, 749–752 (2013).
15. S. Tatur, M. Maccarini, R. Barker, A. Nelson, G. Fragneto, Effect of functionalized gold nanoparticles on floating lipid bilayers. *Langmuir* **29**, 6606–6614 (2013).
16. D. P. Cormode *et al.*, Nanocrystal core high-density lipoproteins: A multimodality contrast agent platform. *Nano Lett.* **8**, 3715–3723 (2008).
17. I. E. Allijn *et al.*, Gold nanocrystal labeling allows low-density lipoprotein imaging from the subcellular to macroscopic level. *ACS Nano* **7**, 9761–9770 (2013).
18. Z. Shen *et al.*, Self-assembly of core-polyethylene glycol-lipid shell (CPLS) nanoparticles and their potential as drug delivery vehicles. *Nanoscale* **8**, 14821–14835 (2016).
19. P. Li, D. Li, L. Zhang, G. Li, E. Wang, Cationic lipid bilayer coated gold nanoparticles-mediated transfection of mammalian cells. *Biomaterials* **29**, 3617–3624 (2008).
20. An X, Naowarojna N, Liu P, & Reinhard BM, Hybrid plasmonic photoreactors as visible light-mediated bactericides. *ACS Appl. Mater. Interfaces* **12**, 106–116 (2020).
21. D. Pornpattananangkul *et al.*, Bacterial toxin-triggered drug release from gold nanoparticle-stabilized liposomes for the treatment of bacterial infection. *J. Am. Chem. Soc.* **133**, 4132–4139 (2011).
22. B. Eshaghi *et al.*, Stiffness of HIV-1 mimicking polymer nanoparticles modulates ganglioside-mediated cellular uptake and trafficking. *Adv. Sci. (Weinh.)* **7**, 2000649 (2020).
23. R. Mei, Y. Wang, W. Liu, L. Chen, Lipid bilayer-enabled synthesis of Waxberry-like core-fluidic satellite nanoparticles: Toward ultrasensitive surface-enhanced Raman scattering tags for bioimaging. *ACS Appl. Mater. Interfaces* **10**, 23605–23616 (2018).
24. A. Bandara, A. Panahi, G. A. Pantelopulos, J. E. Straub, Exploring the structure and stability of cholesterol dimer formation in multicomponent lipid bilayers. *J. Comput. Chem.* **38**, 1479–1488 (2017). Correction in: *J. Comput. Chem.* **40**, 2348 (2019).
25. M. R. Elkins, A. Bandara, G. A. Pantelopulos, J. E. Straub, M. Hong, Direct observation of cholesterol dimers and tetramers in lipid bilayers. *J. Phys. Chem. B* **125**, 1825–1837 (2021).
26. G. Saher *et al.*, High cholesterol level is essential for myelin membrane growth. *Nat. Neurosci.* **8**, 468–475 (2005).
27. H. Ohvo-Rekilä, B. Ramstedt, P. Leppimäki, J. P. Slotte, Cholesterol interactions with phospholipids in membranes. *Prog. Lipid Res.* **41**, 66–97 (2002).
28. A. Bandara, A. Panahi, G. A. Pantelopulos, T. Nagai, J. E. Straub, Exploring the impact of proteins on the line tension of a phase-separating ternary lipid mixture. *J. Chem. Phys.* **150**, 204702 (2019).
29. G. A. Pantelopulos, T. Nagai, A. Bandara, A. Panahi, J. E. Straub, Critical size dependence of domain formation observed in coarse-grained simulations of bilayers composed of ternary lipid mixtures. *J. Chem. Phys.* **147**, 095101 (2017).
30. X. L. Guan *et al.*, Functional interactions between sphingolipids and sterols in biological membranes regulating cell physiology. *Mol. Biol. Cell* **20**, 2083–2095 (2009).
31. K. Bacia, P. Schwille, T. Kurzchalia, Sterol structure determines the separation of phases and the curvature of the liquid-ordered phase in model membranes. *Proc. Natl. Acad. Sci. U.S.A.* **102**, 3272–3277 (2005).
32. M. M. Gleason, M. S. Medow, T. N. Tulenko, Excess membrane cholesterol alters calcium movements, cytosolic calcium levels, and membrane fluidity in arterial smooth muscle cells. *Circ. Res.* **69**, 216–227 (1991).
33. S. Tian *et al.*, Polydiacetylene-based ultrastrong bioorthogonal Raman probes for targeted live-cell Raman imaging. *Nat. Commun.* **11**, 81 (2020).
34. Z. Chen *et al.*, Multicolor live-cell chemical imaging by isotopically edited alkyne vibrational palette. *J. Am. Chem. Soc.* **136**, 8027–8033 (2014).
35. F. Boeck, T. Kribber, L. Xiao, L. Hintermann, Mixed phosphane η5-CpRuCl(PR3)2 complexes as ambifunctional catalysts for anti-Markovnikov hydration of terminal alkynes. *J. Am. Chem. Soc.* **133**, 8138–8141 (2011).
36. F. L. Hirshfeld, Bonded-atom fragments for describing molecular charge densities. *Theor. Chim. Acta* **44**, 129–138 (1977).
37. A. M. Smondyrev, M. L. Berkowitz, Structure of dipalmitoylphosphatidylcholine/cholesterol bilayer at low and high cholesterol concentrations: Molecular dynamics simulation. *Biophys. J.* **77**, 2075–2089 (1999).
38. N. M. Rao, A. L. Plant, V. Silin, S. Wight, S. W. Hui, Characterization of biomimetic surfaces formed from cell membranes. *Biophys. J.* **73**, 3066–3077 (1997).
39. H. Fan *et al.*, Self-assembly of ordered, robust, three-dimensional gold nanocrystal/silica arrays. *Science* **304**, 567–571 (2004).
40. J. E. Moses, A. D. Moorhouse, The growing applications of click chemistry. *Chem. Soc. Rev.* **36**, 1249–1262 (2007).
41. E. M. M. Manders, F. J. Verbeek, J. A. Aten, Measurement of co-localization of objects in dual-colour confocal images. *J. Microsc.* **169**, 375–382 (1993).
42. J. R. Matthews, C. R. Shirazinejad, G. A. Isakson, S. M. E. Demers, J. H. Hafner, Structural analysis by enhanced Raman scattering. *Nano Lett.* **17**, 2172–2177 (2017).
43. H. J. Hughes, S. M. E. Demers, A. Zhang, J. H. Hafner, The orientation of a membrane probe from structural analysis by enhanced Raman scattering. *Biochim. Biophys. Acta Biomembr.* **1862**, 183109 (2020).
44. D. Marquardt, N. Kučerka, S. R. Wassall, T. A. Harroun, J. Katsaras, Cholesterol's location in lipid bilayers. *Chem. Phys. Lipids* **199**, 17–25 (2016).
45. T. A. Harroun, J. Katsaras, S. R. Wassall, Cholesterol hydroxyl group is found to reside in the center of a polyunsaturated lipid membrane. *Biochemistry* **45**, 1227–1233 (2006).
46. S. R. Shaikh *et al.*, Molecular organization of cholesterol in unsaturated phosphatidylethanolamines: X-ray diffraction and solid state 2H NMR reveal differences with phosphatidylcholines. *J. Am. Chem. Soc.* **128**, 5375–5383 (2006).
47. S. J. Marrink, A. H. de Vries, T. A. Harroun, J. Katsaras, S. R. Wassall, Cholesterol shows preference for the interior of polyunsaturated lipid membranes. *J. Am. Chem. Soc.* **130**, 10–11 (2008).
48. J. S. Allhusen, D. R. Kimball, J. C. Conboy, Structural origins of cholesterol accelerated lipid flip-flop studied by sum-frequency vibrational spectroscopy. *J. Phys. Chem. B* **120**, 3157–3168 (2016).
49. T. Róg, L. M. Stimson, M. Pasenkiewicz-Gierula, I. Vattulainen, M. Karttunen, Replacing the cholesterol hydroxyl group with the ketone group facilitates sterol flip-flop and promotes membrane fluidity. *J. Phys. Chem. B* **112**, 1946–1952 (2008).
50. C. Reichardt, T. Welton, *Solvents and Solvent Effects in Organic Chemistry* (John Wiley & Sons, 2011).
51. P. L. Stiles, J. A. Dieringer, N. C. Shah, R. P. Van Duyne, Surface-enhanced Raman spectroscopy. *Annu. Rev. Anal. Chem. (Palo Alto, Calif.)* **1**, 601–626 (2008).
52. R. Goul *et al.*, Quantitative analysis of surface enhanced Raman spectroscopy of Rhodamine 6G using a composite graphene and plasmonic Au nanoparticle substrate. *Carbon* **111**, 386–392 (2017).

53. K. Zhang *et al*., An improved approach to prepare triazole protective film by click-assembly on copper surface. *Corros. Sci.* **164**, 108352 (2020).
54. K. Larsson, R. P. Rand, Detection of changes in the environment of hydrocarbon chains by Raman spectroscopy and its application to lipid-protein systems. *Biochim. Biophys. Acta* **326**, 245–255 (1973).
55. M. Doğangün *et al*., Hydrogen-bond networks near supported lipid bilayers from vibrational sum frequency generation experiments and atomistic simulations. *J. Phys. Chem. B* **122**, 4870–4879 (2018).
56. N. Dalchand *et al*., Perturbation of hydrogen-bonding networks over supported lipid bilayers by poly (allylamine hydrochloride). *J. Phys. Chem. B* **123**, 4251–4257 (2019).
57. C. Leng *et al*., Probing the surface hydration of nonfouling zwitterionic and PEG materials in contact with proteins. *ACS Appl. Mater. Interfaces* **7**, 16881–16888 (2015).
58. A. Srivastava, A. Debnath, Hydration dynamics of a lipid membrane: Hydrogen bond networks and lipid-lipid associations. *J. Chem. Phys.* **148**, 094901 (2018).
59. M. Hu, F. Stanzione, A. K. Sum, R. Faller, M. Deserno, Design principles for nanoparticles enveloped by a polymer-tethered lipid membrane. *ACS Nano* **9**, 9942–9954 (2015).
60. H. Abramczyk, B. Brozek-Pluska, Raman imaging in biochemical and biomedical applications. Diagnosis and treatment of breast cancer. *Chem. Rev.* **113**, 5766–5781 (2013).
61. H. Yamakoshi *et al*., Imaging of EdU, an alkyne-tagged cell proliferation probe, by Raman microscopy. *J. Am. Chem. Soc.* **133**, 6102–6105 (2011).
62. J. Filmus, M. N. Pollak, R. Cailleau, R. N. Buick, MDA-468, a human breast cancer cell line with a high number of epidermal growth factor (EGF) receptors, has an amplified EGF receptor gene and is growth inhibited by EGF. *Biochem. Biophys. Res. Commun.* **128**, 898–905 (1985).
63. S. L. Fitzpatrick, M. P. LaChance, G. S. Schultz, Characterization of epidermal growth factor receptor and action on human breast cancer cells in culture. *Cancer Res.* **44**, 3442–3447 (1984).
64. J. A. Berkers, P. M. van Bergen en Henegouwen, J. Boonstra, Three classes of epidermal growth factor receptors on HeLa cells. *J. Biol. Chem.* **266**, 922–927 (1991).
65. J. Qi *et al*., Boosting fluorescence-photoacoustic-Raman properties in one fluorophore for precise cancer surgery. *Chem* **5**, 2657–2677 (2019).
66. Z.-L. Song *et al*., Alkyne-functionalized superstable graphitic silver nanoparticles for Raman imaging. *J. Am. Chem. Soc.* **136**, 13558–13561 (2014).
67. W. J. Tipping, M. Lee, A. Serrels, V. G. Brunton, A. N. Hulme, Imaging drug uptake by bioorthogonal stimulated Raman scattering microscopy. *Chem. Sci.* **8**, 5606–5615 (2017).
68. L. Martínez, R. Andrade, E. G. Birgin, J. M. Martínez, PACKMOL: A package for building initial configurations for molecular dynamics simulations. *J. Comput. Chem.* **30**, 2157–2164 (2009).
69. K. Vanommeslaeghe *et al*., CHARMM general force field: A force field for drug-like molecules compatible with the CHARMM all-atom additive biological force fields. *J. Comput. Chem.* **31**, 671–690 (2010).
70. J. B. Klauda *et al*., Update of the CHARMM all-atom additive force field for lipids: Validation on six lipid types. *J. Phys. Chem. B* **114**, 7830–7843 (2010).
71. W. L. Jorgensen, J. Chandrasekhar, J. D. Madura, R. W. Impey, M. L. Klein, Comparison of simple potential functions for simulating liquid water. *J. Chem. Phys.* **79**, 926–935 (1983).
72. S. Jo *et al*., CHARMM-GUI 10 years for biomolecular modeling and simulation. *J. Comput. Chem.* **38**, 1114–1124 (2017).
73. M. J. Abraham *et al*., GROMACS: High performance molecular simulations through multi-level parallelism from laptops to supercomputers. *SoftwareX* **1–2**, 19–25 (2015).
74. S. Bolte, F. P. Cordelières, A guided tour into subcellular colocalization analysis in light microscopy. *J. Microsc.* **224**, 213–232 (2006).